

Resonant neutralization of H^- near Cu surfaces: Effects of the surface symmetry and ion trajectory

Himadri Chakraborty,* Thomas Niederhausen, and Uwe Thumm†

James R. Macdonald Laboratory, Department of Physics, Kansas State University, Manhattan, Kansas 66506-2604, USA

(Received 15 July 2003; revised manuscript received 13 May 2004; published 23 November 2004)

A comparative study of the resonant charge-transfer process of H^- in front of plane-model Cu surfaces of symmetries (111) and (100) is performed using a two-dimensional Crank-Nicholson wave-packet propagation approach. Very different electron evolutions near the two surfaces are related to different structures of the respective band gaps and allow for the visualization of electronic interaction mechanisms. It is shown that electrons get localized near the Cu(111) surface due to the reflectivity imposed by the band gap. This enables considerable recapture by the ion. In contrast, H^- is neutralized more efficiently near Cu(100), for which the surface state is embedded in the bulk valence band. Image states are found to be important intermediaries for charge transfer at smaller ion-surface distances. As a consequence of all these effects, the dynamics of ion neutralization near (111) and (100) surfaces vastly differ to yield quite dissimilar ion-survival probabilities. It is found that while the ion-surface interaction time becomes important at normal incidence, for near-grazing incidences, the point of closest approach to the surface is a crucial determinant of the ion survival.

DOI: 10.1103/PhysRevA.70.052903

PACS number(s): 79.20.Rf, 34.70.+e, 73.20.At

I. INTRODUCTION

The investigation of electron transfer and associated orbital hybridization processes during the interaction of a projectile atom or ion with a metal surface is of fundamental and practical importance. The ensuing knowledge finds valuable use in various applied fields of physics, such as the development of ion sources, control of ion-wall interactions in fusion plasma, surface chemistry and analysis, secondary-ion mass spectroscopy, reactive ion etching, and semiconductor miniaturization via thin-film deposition [1,2].

In order to understand the effect of band structures on the charge transfer near a metal surface, a diverse range of projectiles and target surfaces has been considered for experimental studies within the past decade. This includes the Auger neutralization of He^+ under grazing incidences on a flat Ag(111) surface [3], the transfer and tunneling dynamics of Xe Rydberg atoms incident onto a Au(111) surface [4], the nonresonant localized charge-exchange mechanism in H, O, and F and their anions in front of a MgO(100) surface [5], the effect of stepped structures on the Pt surface in its interaction with fast N^{6+} and N^{7+} ions [6], and the delocalization of the so-called dangling-bond surface states in fast Li^+ scattering from covered Si surfaces [7].

Of basic interest in our work is the detailed and microscopic description of the single-electron transfer leading to either ionization or neutralization of a surface-scattered projectile. This process of resonant charge transfer (RCT) has been the focus of a number of experimental studies [7–14]. It has been observed [8,9], following a theoretical prediction [15,16], that RCT in ion-surface interactions is strongly influenced by the projected band gap of the metal. This is because the gap impedes the electron penetration normal to

the surface, which is the direction favored by RCT. On the other hand, a variation in the crystallographic symmetry of the surface can alter the substrate electronic structure significantly while the band gap may still exist. This may considerably influence the transfer dynamics. However, although a study of Cu(111) is already published [16], no comparative investigation has yet been made to examine the relative effect of the altering surface symmetry on the charge-transfer dynamics with possible measurable consequences on reflected ion fractions.

The interaction of H^- with Cu surfaces of symmetries (111) and (100) is of interest for a number of reasons: (i) as the ion approaches the surface, the affinity level of H^- shifts across and “explores” the band gap; (ii) these surfaces serve as prototype targets that, respectively, *can* and *cannot* localize a surface state within the band gap; and (iii) the image states are structurally so dissimilar for these two surfaces that they are capable of triggering very different decay patterns during the neutralization of H^- .

We carry out a theoretical investigation of H^- ions impinging on Cu(111) and Cu(100). Our calculation is based on a two-dimensional model that limits the motion of the active electron to the scattering plane of the projectile. Besides quantifying the effect of surface reflectivity and associated density of states on the electron transfer dynamics, we also discuss the importance of image states at close ion-surface distances—an aspect that has not been addressed before. Further, the projectile’s distance of closest approach to the surface is determined by the initial velocity of the ion normal to the surface and the ion-surface repulsive interaction. The projectile decelerates near the surface and the effective interaction time depends sensitively on the trajectory. In contrast to previous work [16], where the influence of the ion-surface interaction on the projectile motion was omitted by restricting the ion to move along a straight-line segment of the incident trajectory, our calculations extend over the full trajectory of the surface-scattered projectile.

*Electronic address: himadri@phys.ksu.edu

†Electronic address: thumm@phys.ksu.edu

A fundamental aspect of the microscopic description of RCT dynamics is the understanding of the formation of transient electronic states of adsorbates and how these excited states couple to inelastic decay channels. For example, an enhancement of the cross section for excited resonance formation caused by the coupling of adsorbed molecular states to the resonant image states of Ag(111) was predicted [17]. Also, it has been observed that the inelastic decay time of photoexcited Cs adsorbed on Cu(111) (15 ± 6 fs) [18,20] is longer than that for Cu(100) (6 ± 4 fs) [18]. A theoretical interpretation of this result has already been given on the basis of Cu-surface electronic structures [19]. Further, unusually strong normal binding energies of Xe on Pd(111) (320 ± 10 meV) [21] and on Pt(111) (260 ± 15 meV) [22] have been found very recently and attributed to, respectively, the unoccupied and partially occupied Shockley surface state. In a different process, it has been speculated that the so-called anticorugation effects, which arise in the He scattering off Ni(110) and Cu(110), are related to localized surface states [23].

Theoretically, RCT has been addressed by employing several nonperturbative methods, including single-center basis-set expansion [24], complex coordinates rotation [25], two-center expansion [26], multicenter expansion techniques [27], and the direct numerical integration of the effective single-electron Schrödinger equation by Crank-Nicholson wave-packet propagation (CNP) [15,16,28]. Among these methods, CNP [29] is the most flexible in the sense that it can readily be applied to any parametrized effective potential that may be used to represent the electronic structure of substrate and projectile. In contrast to expansion methods, which usually simplify the target to a free-electron (jellium) metal, CNP allows for a significantly more detailed representation of the substrate electronic structure, including the effect of band gaps [8,15], surface states [16], and image states on the RCT dynamics.

So far, the vast majority of *ab initio* charge-transfer studies for particle-surface scattering were restricted to one active electron. For CNP calculations, in particular, the demand on available computing resources increases rapidly with the dimensionality of the model system, and many-electron effects have not yet been included from the outset. For this reason, the appealing flexibility of CNP with regard to the choice of parametrized electronic potentials is in part offset by the exclusion of quantum statistical effects, such as the Pauli principle.

In the following section, we detail the model potentials and highlight some important aspects of our CNP methodology. Section III presents a discussion of our results. We summarize the results and make relevant remarks in the concluding section. Unless indicated otherwise we use atomic units.

II. ESSENTIAL THEORETICAL DETAILS

A. Potentials

We model the Cu(111) and Cu(100) surface by a one-dimensional (1D) [in the coordinate (z) along the surface normal] semiempirical single-electron effective potential,

constructed from pseudopotential local density calculations [31],

$$V_{\text{surf}}(z) = V_1(z) + V_2(z) + V_3(z) + V_4(z), \quad (1)$$

where

$$V_1(z) = A_{10} + A_1 \cos\left(\frac{2\pi}{a_s} z\right), \quad |z| < d/2, \quad (2a)$$

$$V_2(z) = -A_{20} + A_2 \cos[\beta(z - d/2)], \quad d/2 < |z| < z_1, \quad (2b)$$

$$V_3(z) = A_3 \exp[-\alpha(z - z_1)], \quad z_1 < |z| < z_{\text{im}}, \quad (2c)$$

$$V_4(z) = 27.21 \text{ eV} \frac{\exp[-\lambda(z - z_{\text{im}})] - 1}{4(z - z_{\text{im}})}, \quad z_{\text{im}} < |z|. \quad (2d)$$

To find an optimum size of our grid for a good representation of the bulk, surface, and vacuum, we proceed as follows. We consider a Cu slab of 200 Cu atoms separated by the lattice constant a_s [$=3.940a_0$ for Cu(111) and $=3.415a_0$ for Cu(100)] with d in the above equations being the width of the Cu slab, which is symmetric about $z=0$. Inside the bulk region $V_{\text{surf}}(z)$ is periodic [Eq. (2a)]. Across the metal-surface interface, $V_{\text{surf}}(z)$ transforms through Eqs. (2b) and (2c) to a screened Coulomb potential, Eq. (2d), that goes over to a pure hydrogenic form at large distances from the surface on the vacuum side. Following Ref. [31], the set of four independent parameters in Eq. (2) for both surfaces is

	A_{10} (eV)	A_1 (eV)	A_2 (eV)	$\beta(a_0^{-1})$
Cu(111)	-11.895	5.14	4.3279	2.9416
Cu(100)	-11.480	6.10	3.7820	2.5390

The remaining six parameters are determined by enforcing continuity of the logarithmic derivative of the potential everywhere in space. The parameter z_{im} , which defines the image plane position, is $\pm(d/2 + 2.106a_0)$ for Cu(111) and $\pm(d/2 + 2.273a_0)$ for Cu(100). Including a $200a_0$ -wide vacuum on either side of the slab, we diagonalize the potential with a grid spacing of 0.2 a.u. The diagonalization on such a grid reproduces the projected band gap, surface-state energy, and image-state energies known from first-principles calculations and/or experimental data (an account of these known results is given in Ref. [31]).

The potentials and the relevant wave functions and energies (relative to the vacuum) obtained are shown in Fig. 1. Owing to two surface layers at $z = \pm d/2$ of our slab, the diagonalization yields wave functions of gerade and ungerade symmetry. We show in Fig. 1 the states appearing near the surface plane at $z = d/2$. Cu(111) and Cu(100) exhibit very different electronic structures. For Cu(111) [Fig. 1(a)], a projected L -band gap exists between $E_a = -0.70$ eV and $E_b = -5.93$ eV. A surface state at $E_s = -5.33$ eV occurs inside this gap which indicates a strong surface localization by an exponentially decaying oscillation into the bulk and very

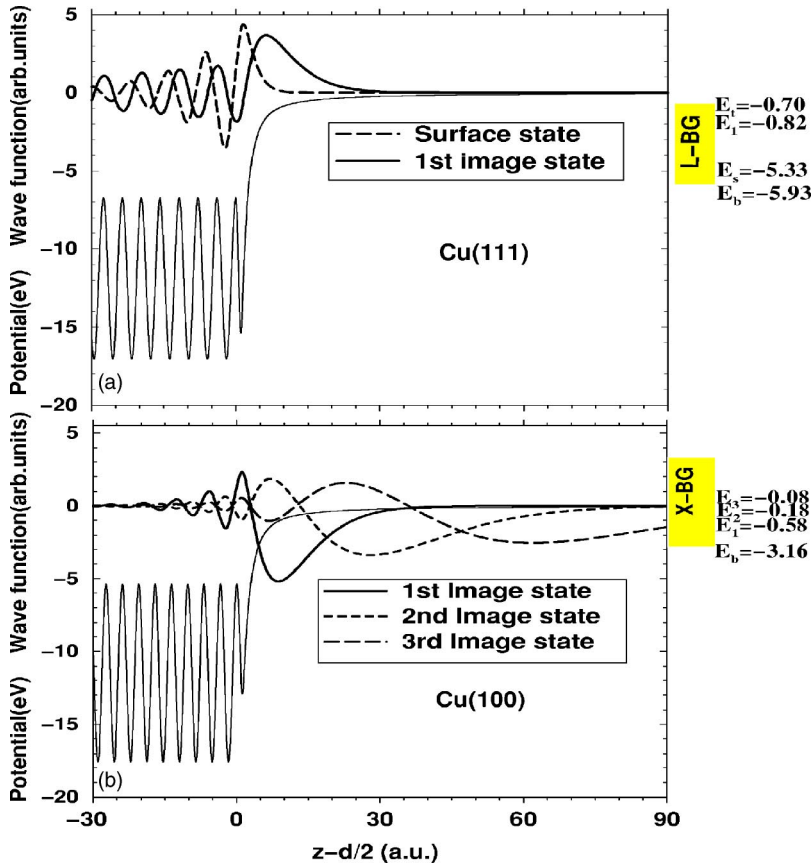


FIG. 1. Surface potentials and local wave functions for (a) Cu(111) and (b) Cu(100). The parameter d is as in Eq. (2).

rapid decrease on the vacuum side. The first image state at $E_1 = -0.82$ eV lies barely in the band gap while higher ones are degenerate with the conduction band.

In contrast, the Cu(100) surface [Fig. 1(b)] has the X-band gap bottom at $E_b = -3.16$ eV, but the gap extends beyond the vacuum energy. While no surface state occurs in the band gap, a surface state is found degenerate with the valence band. On the numerical grid considered here, the Cu(100) effective potential can support five image states out of which the energies ($E_1 = -0.58$ eV, $E_2 = -0.18$ eV, $E_3 = -0.084$ eV) and the wave functions [Fig. 1(b)] of the first three states in our diagonalization agree with Ref. [31]. The valence and conduction bands of Cu(111) and Cu(100) are reproduced in our diagonalization in terms of a large number of bound (discretized) bulk states [32]

We construct a jellium potential to represent the ideal free-electron surface, with the same long-range behavior of Eq. (1), according to

$$V_{\text{jell}}(z) = V_0(z) + V_3(z) + V_4(z), \quad (3)$$

where

$$V_0(z) = \frac{A_{10}}{1 + A \exp[B(z - z_1)]}, \quad |z| < z_1, \quad (4)$$

is of the form given by Jennings *et al.* [33]; V_3 and V_4 are the same as before [Eqs. (2c) and (2d)]. For consistency, we chose the average of 11.895 eV [A_{10} for Cu(111)] and 11.480 eV [A_{10} for Cu(100)] to be the value of A_{10} in our jellium calculations. The parameters A and B are determined from

the requirement of continuity of the potential.

The H^- ion is described by a spherically symmetric effective single-electron potential that models the interaction of the active electron with a polarizable core [34]:

$$U(r) = -(1 + 1/r)\exp(-2r) - (a/2r^4)\exp(-b/r^2). \quad (5)$$

In order to ensure good numerical accuracy for small radial coordinates, we regularize this potential according to [16,35]

$$V_{\text{ion}} = \frac{\gamma U}{\sqrt{\mu U^2 + 1}}. \quad (6)$$

Here r denotes the distance from the hydrogen core, whose polarizability a is $4.5a_0^3$. The parameter b is set to $2.547a_0^2$. On a 3D grid ($r = \sqrt{x^2 + y^2 + z^2}$), $\mu = 0.1156$ and $\gamma = 1.107$ yield an electron affinity of 0.76 eV. To suit our reduced-dimensionality calculations, we reparametrized μ and γ for the 2D ($\mu = 0.1417$, $\gamma = 0.3923$) and 1D ($\mu = 0.1417$, $\gamma = 0.0888$) H^- ions in order to ensure the same electron affinity.

B. Electronic propagation

We employ the CNP [28,29] of the initial free H^- wave function $\phi_{\text{ion}}(\vec{r})$ over a 2D numerical grid in which the metal continuum is approximated by free electronic motion in the x direction, parallel to the surface. The time-dependent electronic wave function $\Phi(\vec{r}, t)$ is a solution of the time-dependent Schrödinger equation with Hamiltonian

$$H = H' + H_{\text{free}}, \quad (7)$$

where

$$H' = -\frac{1}{2} \frac{d^2}{dz^2} + V_{\text{ion}} + V_{\text{surf}}, \quad (8a)$$

$$H_{\text{free}} = -\frac{1}{2} \frac{d^2}{dx^2}. \quad (8b)$$

Since the topmost layer of lattice points defines $z=0$, we set $d=0$ in Eq. (2). For fixed ion-surface distances D , the numerical propagation over time t yields

$$\Phi(\vec{r}, t + \Delta t; D) = \exp[-iH(D)\Delta t]\Phi(\vec{r}, t; D), \quad (9)$$

with the initial wave packet $\Phi(\vec{r}, t=0; D) = \phi_{\text{ion}}(\vec{r}; D)$. The time-evolution operator is approximated by the usual split-operator technique as

$$\begin{aligned} \exp(-iH\Delta t) &\approx \exp(-iH_{\text{free}}\Delta t/2)\exp(-iH'\Delta t) \\ &\times \exp(-iH_{\text{free}}\Delta t/2). \end{aligned} \quad (10)$$

The unitary and unconditionally stable Cayley scheme [29] is used to evaluate the exponential operators in Eq. (10).

For sufficient numerical accuracy, we construct a grid which includes 100 layers on the bulk (one-half the size of the previously diagonalized symmetric slab) and extends to $z=200$ on the vacuum side. We use the same grid spacing $\Delta z=0.2$, as before. The grid extends from $x=-160$ to $x=160$ in the parallel direction with Δx being equal to 0.3. The operators are discretized over this grid using a three-point differentiation formula and the Crank-Nicholson scheme is applied by diagonalization of a tridiagonal matrix in order to obtain $\Phi(\vec{r}, t)$ at every time step [29].

The ionic survival amplitude (autocorrelation) is thus calculated as

$$A(t) = \langle \Phi(\vec{r}, t) | \phi_{\text{ion}}(\vec{r}) \rangle. \quad (11)$$

The real part of the Fourier transform (FT) of this amplitude yields the projected density of states (PDOS), which exhibits resonance structures corresponding to various localized states. The position, width [full width at half maximum (FWHM)], and amplitude of these resonances provide, respectively, the energy, lifetime, and population of the states. The FT of $A(t)$ is performed by propagating over a period long enough to ensure ‘‘complete neutralization.’’ In this context, ‘‘long enough’’ means that the wave function is propagated until $A(t)$ becomes practically zero, implying a total departure of the electron from the ion. For smaller D (≤ 10), the ionization is relatively fast, requiring a propagation time of $\leq 16\,000$. For larger D , however, proportionately longer propagation times were needed. The resonance energies and widths are found converged for time steps $\Delta t=0.1$.

In order to avoid unphysical reflections of outgoing electron flux from grid boundaries and thereby imposing an outgoing-wave behavior for the wave packet, we employ absorbers at the grid edges [30]. At each time step we multiply the wave packet inside an absorber by a masking function of the form $\exp(-s|\rho - \rho_0|^n \Delta t)$, where ρ is the coordinate, and ρ_0 and s are, respectively, the starting edge and the strength of

the absorber. Moving into the bulk along $-z$, the wave packet gradually spreads over available bulk states, which decay freely in the parallel direction. Hence, a small amount of electrons with a fairly large velocity, due to their steep descent to the mean position A_{10} of the corrugated potential, can finally reach the grid edge. We used a cubic ($n=3$) absorber of a width of 15 and $s=5 \times 10^{-4}$ in the $-z$ direction. However, when image states and/or conduction-band states interact with the ion, electrons move rather slowly along the $+z$ direction. Further, since the minimum possible energy differences between the ion level and the surface state and between the surface state and the top of the valence band are rather small, electrons that propagate parallel to the surface may have very small velocities. Hence, quadratic absorbers ($n=2$) at the grid edges along the $+z$ and $\pm x$ directions with a large width of 100 and $s=4.93 \times 10^{-6}$ were required.

The propagation over a 1D grid along z —i.e., neglecting the electronic motion parallel to the surface—does not yield converged amplitudes $A(t)$. This is because, in the absence of decay continua, both the affinity level and (111) surface state are degenerate with the band gap and become stationary (with zero width). In practice, however, the FT of the 1D amplitude always shows a very small and artificial width for these states owing to absorptions at grid boundaries. For the (100) surface state embedded in the valence band, on the other hand, decay in the z direction is possible and, therefore, even the 1D propagation shows a finite width of the corresponding resonance. With these in mind, we calculated the 1D PDOS in order to provide the energies of all states, while attributing physical meaning to the width of surface state resonance for Cu(100) only.

C. Projectile trajectory

In Sec. III A (below), we keep the H^- ion at a fixed distance D from the surface and ignore the short-range repulsion between the projectile core and the surface. We include this interaction in our calculations for the moving ion (Sec. III B). Sufficiently close to the surface the ion gradually decelerates in the normal direction along its incoming trajectory, owing to the repulsive interaction between its core and surface atoms. As a result, the normal velocity (v_{nor}) of the ion becomes zero at the point of closest approach (D_{cls}). For specular reflection, the ion regains its original normal velocity. For a given initial asymptotic kinetic energy and angle of incidence, we simulate the classical ion trajectory by modeling the core-surface interaction via a plane-averaged ‘‘Biersack-Ziegler’’ interatomic potential $U^{BZ}(z)$ [36]. This defines a distance of closest approach as a function of the initial normal velocity $v_{\text{nor}}^{\text{in}}$. (We have verified that the ion-surface image interaction does not have any significant effect on the trajectory.) For translationally invariant surfaces, the parallel velocity of the ion along the trajectory remains constant and equal to its asymptotic value $v_{\text{par}}^{\text{in}}$. This invariance ensures that the dynamics is free of any parallel velocity effect. The ionic motion is then incorporated in the electronic propagation by adding the translational phase corresponding to v_{nor} . This is done by multiplying the initial wave packet by $\exp[-i(v_{\text{nor}}z + v_{\text{nor}}^2 t/2)]$. We find the ionic survival probability

long after the ion's scattering from the surface as $\lim_{t \rightarrow \infty} |A(t)|^2$. The initial ion position is taken as 50 a.u. from the surface where the ion can be considered as free. Similarly, when the reflected ion reaches a distance of 50 a.u. from the surface, we assume that charge transfer has stopped.

III. RESULTS AND DISCUSSIONS

A. Results for propagation with a fixed ion

The positions and widths of resonances in the PDOS, obtained via propagation at fixed ion-surface distances, facilitate the explanation of charge transfer from a moving ion. This is true not only for very slow (adiabatic) incident ions, but also for ions with higher energies, since the projectile normal velocity at close ion-surface distances becomes so small that the transfer dynamics practically approximates adiabatic conditions. Hence, we begin this section by describing, in fixed-ion approximation, the differences in PDOS spectra that are due to different surface symmetries.

1. Projected density of states

Figure 2 shows the PDOS for the three typical values of $D=11, 5,$ and 1 for Cu(111). At $D=11$ [Fig. 2(a)], our 2D results (solid curve) with and our 1D results (dashed curve) without the parallel electronic motion included show discretized structures corresponding to the valence- and conduction-band (bulk) states. The positions of the band edges are very well reproduced. By including the free electronic motion in the surface plane, each of the local surface and image states from Eqs. (1) and (2) becomes the bottom of a continuum. While these bottoms do not shift as a result of the localized perturbation exerted by the ion [16,37], new resonances emerge from them which we denote as “surface-state” and “image-state” resonances.

In Fig. 2(a), the affinity-level resonance (denoted as AL in the figure) at -1.56 eV and the surface-state resonance (SS in the figure) at -5.33 eV are present in both 1D and 2D calculations, although the affinity level is shifted downward from the unperturbed asymptotic affinity of -0.76 eV due to the characteristic image interaction. As expected, the PDOS [dash-dotted curve in Fig. 2(a)] for the interaction with free-electron (jellium) Cu only shows the affinity level resonance.

For $D=5$ [Fig. 2(b)], the affinity level and the surface-state resonance are present in both results, with and without parallel motion, at -1.65 eV and -5.42 eV, respectively. The width of the affinity level resonance, when including the parallel motion, is much larger than that in the case of $D=11$. The surface-state resonances from both 1D and 2D propagation move slightly closer to the valence band, while the 2D result clearly shows larger widths. The peak for the jellium case widens significantly at this position of the ion.

For very close ion-surface distance, at $D=1$ [Fig. 2(c)], the 2D surface-state resonance becomes wider. The affinity-level resonance narrows and moves very close to the conduction band. Small resonance structures (IS n in the figure) at -0.77 eV, -0.22 eV, and -0.08 eV are due to the population of, respectively, the first image state (barely in the band gap) and the second and third image states, degenerate with the conduction band [31].

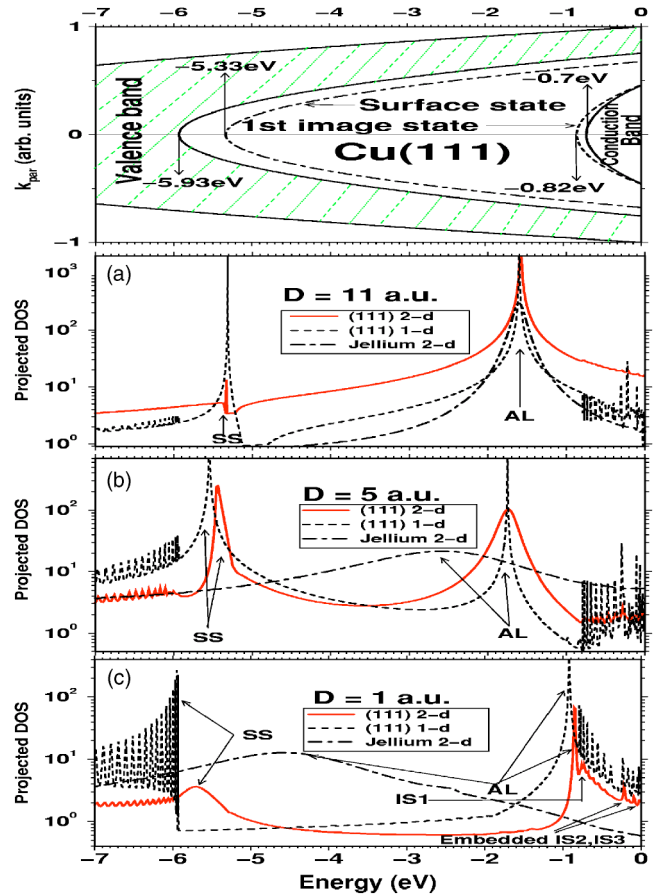


FIG. 2. (Color online) Top panel: schematic of the Cu(111) band structure (relative to the vacuum energy) as a function of k_{par} showing a surface state at -5.33 eV and the first image state at -0.82 eV within the gap separating the valence and conduction bands: (a) PDOS for $D=11$ a.u., (b) $D=5$ a.u., and (c) $D=1$ a.u. The affinity-level, surface-state, and n th image-state resonances are denoted as AL, SS, and IS n , respectively.

Going from $D=11$ to $D=1$, while we note alterations in the decay width of various resonances in the 2D calculation, the grid-edge-absorption-induced 1D widths are extremely small and largely unchanged as a function of D . This indicates that the Cu(111) surface with an L -band gap can efficiently reflect electrons that try to tunnel in along the surface normal. The populated states can only decay if the electron is allowed to have a parallel degree of freedom.

To illustrate how the change in surface symmetry can alter resulting PDOS features, we now look at Fig. 3, which delineates our results for the interaction of H^- with a Cu(100) surface. At an ion-surface separation of 11 [Fig. 3(a)], all three curves exhibit affinity-level resonances around -1.56 eV, with jellium prediction being largest in width. The 1D propagation result produces the lowest three image-state resonances (again denoted as IS n in the figures). For the 2D result, these image-state resonances are a little broader and shift slightly from their positions in the 1D calculation.

Moving closer to the surface, at $D=5$ [Fig. 3(b)], the 2D affinity-level resonance is much wider and shifted energetically upward compared with its 1D counterpart. The 2D image-state resonances also get relatively broader. Interest-

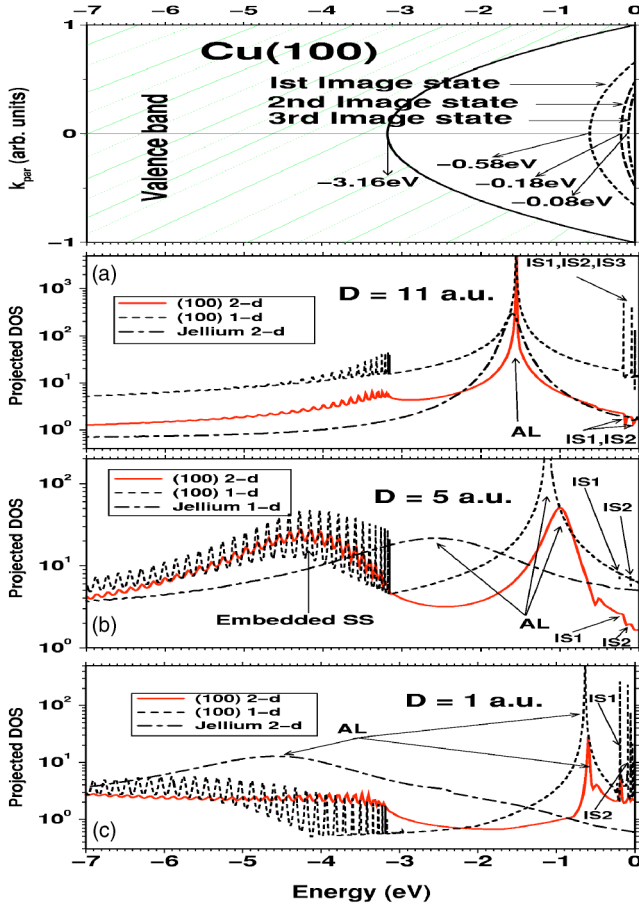


FIG. 3. (Color online) Top panel: schematic of the Cu(100) band structure (relative to the vacuum energy) as a function of k_{par} showing first, second, and third image states at, respectively, -0.58 eV, -0.18 eV, and -0.084 eV within the gap separating the valence and conduction bands: (a) PDOS for $D=11$ a.u., (b) $D=5$ a.u., and (c) $D=1$ a.u. The affinity-level and n th image-state resonances are denoted as AL and IS n , respectively.

ingly, both our 1D and 2D calculations yield a wide bump across the valence band with its peak position at -4.2 eV. This resonance is due to the population of the surface state that is degenerate with the valence band. The similarity between the widths of this resonance for 1D and 2D propagation clearly indicates a predominant decay of this state along the surface normal through the valence band into the Cu(100) bulk.

In Fig. 3(c), at $D=1$ a.u., the embedded surface-state resonance becomes too wide to be identified, the 2D affinity-level resonance becomes a lot narrower, and the image-state resonances in both the 1D and 2D calculations are seen very clearly but with different widths.

2. Surface confinement and electronic density profiles

The existence of a band gap in the direction normal to the surface implies an electron reflectivity of the surface in this direction. This feature is in stark contrast with the jellium surface where the electron is capable of free penetration into the bulk along the surface normal. This reflecting ability of the Cu(111) band gap is so strong that it *can* localize a sur-

face state, whose energy, therefore, falls inside the band gap and whose wave function overlaps weakly with bulk states along the surface normal [Fig. 1(a)]. The Cu(100) gap, on the other hand, can certainly reflect electrons to build up the population of its surface state, but *cannot* localize the state. The surface state becomes embedded in the valence band of Cu(100) [31] and, therefore, decays along the normal direction through its strong coupling with the bulk. This qualitative difference in the surface reflectivity generates an extra propensity for the Cu(111) surface to confine electrons along z in its interaction with the ion as opposed to Cu(100).

Figure 4 illustrates the propagated 2D electron probability densities $|\Phi(\vec{r}, t)|^2$ for $D=5$ for both surfaces. After an elapsed time of 70 [Fig. 4(a)], two distinct and symmetric nodes are formed at $x \sim \pm 10$ just outside the Cu(111) surface (upper panel), while the formation of such nodes is very weak for Cu(100) (lower panel). For Cu(111), this effect is a direct consequence of the band-gap reflection. As soon as the ion-surface interaction begins, the ion first populates the surface state, which is free in the parallel direction. The parallel momentum of the electron $k_{\text{par}}^{\text{ss}}$ from this direct population is determined by the excess energy $E_{\text{AL}} - E_{\text{SS}}$. For $D=5$ [see Fig. 2(b)], $E_{\text{AL}} = -1.65$ eV and $E_{\text{SS}} = -5.42$ eV yield $k_{\text{par}}^{\text{ss}} \sim 0.53$. Due to the surface-state interaction with the bulk, some of the electrons leave the surface state to move further towards the bulk. However, due to the localizing reflectivity of the (111) band gap, these electrons cannot penetrate far into the bulk and stay close to the surface with a parallel momentum $k_{\text{par}}^{\text{vb}} \sim 0.19$ resulting from the difference between E_{SS} and the bottom of the band gap at $E_b = -5.93$ eV. Therefore, after a finite time t , the parallel component of the wave packet near the (111) surface can be approximated as a linear superposition of two momentum components of roughly equal strength:

$$\Phi(x, t) = \psi(t) \exp(ik_{\text{par}}^{\text{ss}} x) + \psi(t) \exp(ik_{\text{par}}^{\text{vb}} x). \quad (12)$$

Quantum interference produces an oscillation with wave number $\Delta k/2 = |k_{\text{par}}^{\text{ss}} - k_{\text{par}}^{\text{vb}}|/2 = 0.17$ in the resulting density:

$$|\Phi(x, t)|^2 = 4|\psi(t)|^2 \cos^2 \frac{\Delta k}{2} x. \quad (13)$$

The corresponding de Broglie half-wavelength $\lambda/2 = \pi/\Delta k = 18.5$ compares well with the distance between two nodes in the upper panel of Fig. 4(a).

The ripples seen in both panels of Fig. 4(a) along the normal direction inside the bulk are due to the population of bulk states. While for Cu(111) the wave front has traveled up to about $z = -40$ in the normal direction, for Cu(100) it has moved further inward up to about $z = -55$, indicating a lesser resistance against bulk penetration for Cu(100). A semicircular and faint blob beyond $z = 10$ for Cu(111) represents a weak population of the image states. Since the second and higher image states are embedded in the conduction band of Cu(111), they decay into the bulk, forming a weakly decaying density flow whose tail is seen at $z < -40$. For Cu(100), electron transfer to the first and second image states is seen occurring with decreasing levels of population.

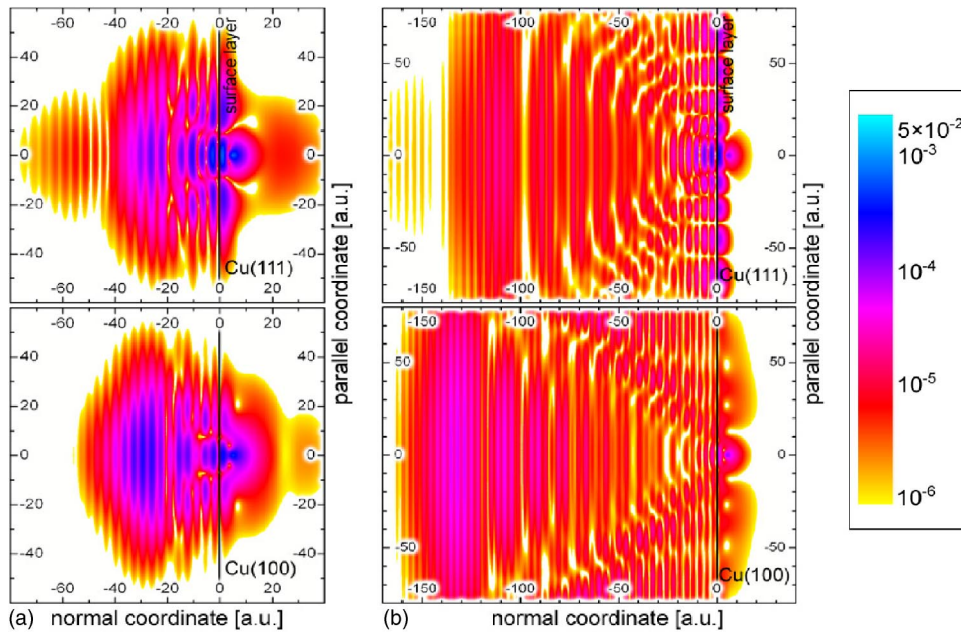
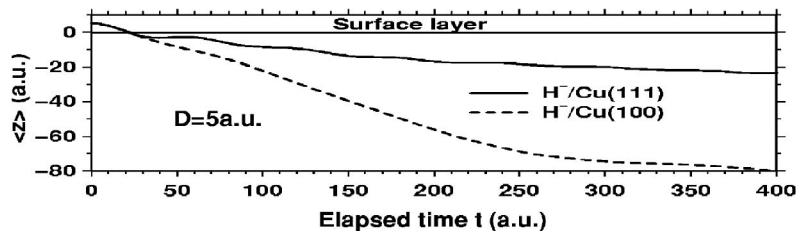


FIG. 4. (Color online) Wave-packet densities (in logarithmic scale) for Cu(111) (upper panel) and Cu(100) (lower panel) at times 70 a.u. (a) and 255 a.u. (b). The propagation is performed by fixing the ion at $D=5$ a.u. The surface position is indicated by a vertical line $z=0$. The ion is situated at $(x=0, z=D)$. Bottom panel: the expectation value of z as a function of the elapsed time.



The difference between Cu(111) and Cu(100) becomes more pronounced at $t=255$ [Fig. 4(b)]. A profound localization of the density at the Cu(111) surface with the formation of several nodes symmetrically along the surface is evident. Again, the typical distance between two successive nodes is in good agreement with our previous estimation of 18.5. Each stack of nodes extends into the bulk up to $z \sim -30$, which is roughly the penetration depth of the surface state [see Fig. 1(a)]. For Cu(100), on the other hand, the high density of the wave front inside the bulk is due to the strong decay of its surface state in the normal direction. The locus of either edge of the moving central wave front for Cu(100) is more inclined towards the normal direction than for Cu(111). This is due to the higher normal velocity of the decaying electron in Cu(100).

To estimate the mean position of the wave packet in the normal direction, we present the expectation value of z , $\langle z \rangle$, as a function of the elapsed time in the bottom panel of Fig. 4. This figure quantifies the localization character of Cu(111) by showing far less bulk penetration of the center of gravity of the electron cloud. At $t=70$ corresponding to Fig. 4(a) for Cu(111), $\langle z \rangle = -3.5$, while $\langle z \rangle = -12$ for Cu(100). At $t=255$ [Fig. 4(b)], it is -18 for Cu(111) and -69.5 for Cu(100).

3. Resonance energies and widths

Figure 5 for Cu(111) depicts the energy and width of various resonances as a function of D . At large distances, the energy [Fig. 5(a)] of the 2D affinity-level resonance (solid

circles) is solely governed by the image interaction $\sim -1/(4D)$ [Eq. (2d)], leading to good agreement with corresponding jellium results (opaque circles). However, moving below $D=8$, the situation drastically alters. While the jellium result keeps moving lower in energy, the affinity-level resonance deviates strongly and shifts upwards. An avoided crossing between the affinity-level and surface-state (solid squares) resonance develops at about $D=6$. As a result, at smaller values of D the affinity-level resonance moves close to the image states (not shown) and the conduction band, while the surface-state resonance shifts towards the valence band. The same adiabatic repulsion of the two interacting states occurs in our 1D propagation results (dashed and dash-dotted lines). For comparison we also display in Fig. 5(a) the affinity-level and surface-state resonance energies of Ref. [16]; the qualitative agreement is good.

A strong interaction between the distance-dependent widths of the affinity-level and surface-state resonances of Cu(111) is evident at $D \leq 8$ when the electron has parallel freedom [Fig. 5(b)]. This is the consequence of an indirect coupling between the corresponding discrete quasistationary states through the surface-state continuum. At $D < 3$, this interaction weakens and the decay via the image states into the metal conduction band becomes important, as Fig. 5(a) suggests. The affinity-level resonance widths for Cu(111) are smaller than the jellium predictions at large distances, since in the jellium case no band gap exists and electrons can decay in the normal direction.

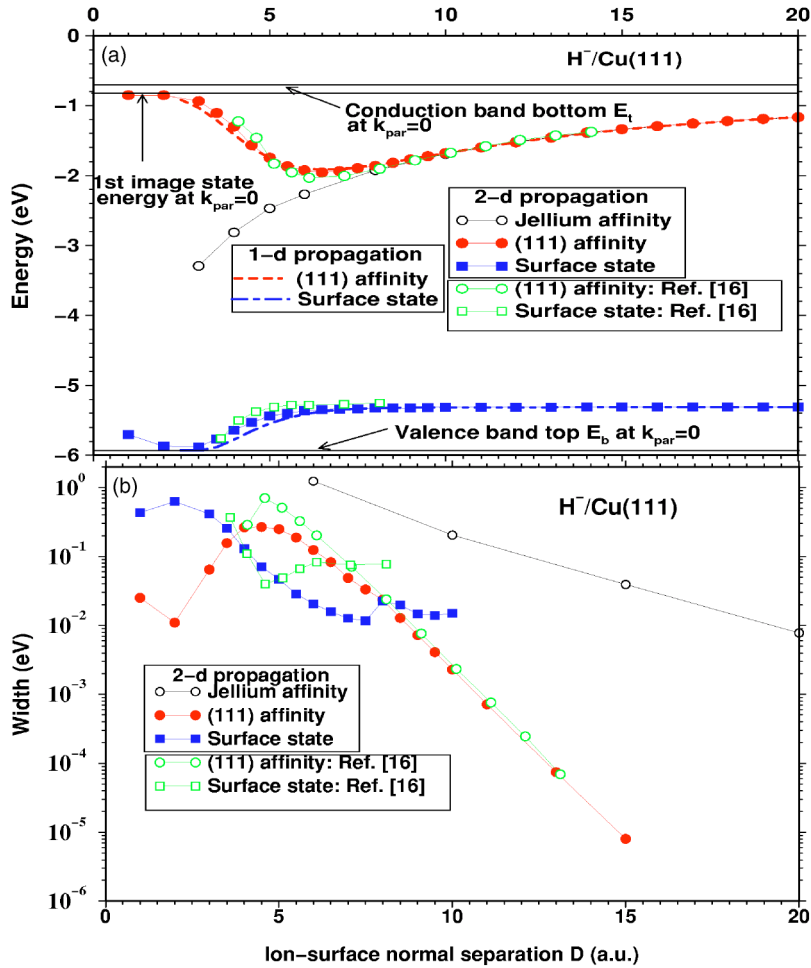


FIG. 5. (Color online) Energies and widths of various resonances as a function of the ion-surface distance for H^- near Cu(111).

Regarding the comparison of our calculated widths with those in Ref. [16], a few comments are necessary. The real decay continuum parallel to the surface is 2D (Cartesian x and y directions in the surface plane). In Ref. [16] a 2D continuum in the parallel direction is employed by adopting a cylindrical coordinate frame. Since we use a 1D parallel continuum instead, for appropriate comparison with our calculated widths, we take one-half of the widths obtained in Ref. [16]. This means that we assume equal decay rates along the two continuum directions such that the added mobility of the active electron along the y direction will double the present width to yield a full 3D result. We then find that the width of our affinity-level resonance near Cu(111) is in good agreement with Ref. [16] for $D \geq 6$ [Fig. 5(b)]. However, the dynamics at smaller D is sensitive to the details of the potentials. Since the shape of the potential used in Ref. [16] is somewhat different at the surface region than the one considered here [Fig. 1(a)], the agreement below $D=6$ worsens for the affinity level. Stronger disagreement for the surface-state resonance may also be attributed to the difference between the potentials in this work and Ref. [16], since the structure of the surface state is far more delicately dependent on the form of the potential at the interface.

In Fig. 6(a), the D -dependent energy of the affinity-level and embedded surface-state resonances of Cu(100) also exhibits a mutual repulsion below $D=8$, both in 1D and 2D calculations. Similar predictions for the embedded surface-

state resonance width for the 1D and 2D propagation in Fig. 6(b) imply that the overlap of this state with valence-band states in the normal direction determines its lifetime. Because of its strong decay in the z direction, the width of the Cu(100) surface-state resonance is much larger than that of Cu(111) [Fig. 5(b)]. The increase in the width of the affinity-level resonance with decreasing D indicates its strong interaction with the embedded surface state. Both 1D and 2D results for the image-state resonance energies show little variation in D , although the 2D resonances are repelled much less strongly in energy [Fig. 6(a)].

In the following subsection we shall demonstrate that these fixed-ion propagation results for resonant energies and widths as a function of the ion-surface separation offer a useful guideline to diagnose the results for ions moving along a classical trajectory.

B. Results for propagation with a moving ion

As mentioned in the Introduction, our one-electron calculations do not enforce the Pauli exclusion principle. It should, therefore, be borne in mind that all electronic states of the two Cu surfaces energetically below the respective Fermi energy are occupied in reality and are not available as final states for the charge transfer. Two-electron mechanisms that could allow for the simultaneous capture into and depletion of an originally occupied substrate state are not included

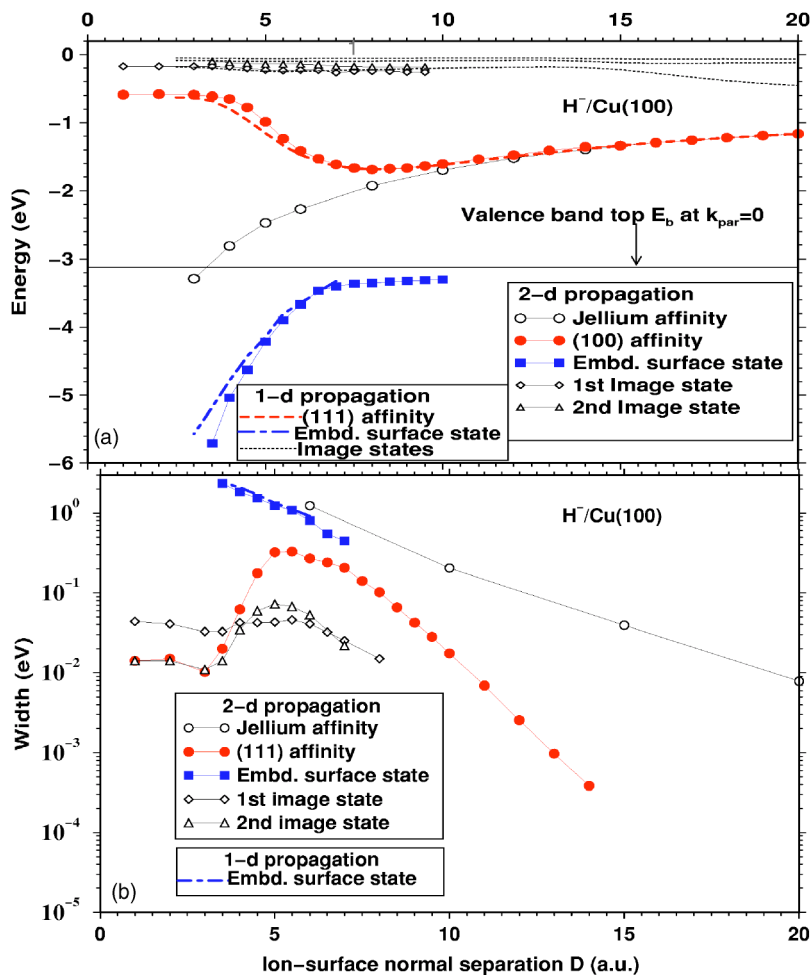


FIG. 6. (Color online) Energies and widths of various resonances as a function of the ion-surface distance for H^- near Cu(100).

in our model. This limitation may not critically affect interactions with Cu(100), whose surface state lies well above the Fermi energy (-5.62 eV). The fact that our simulations allow for neutralization into the surface state of Cu(111), which lies below the Fermi energy (-4.95 eV), is an artifact of the neglect of the ‘‘Pauli blocking.’’ Nevertheless, due to the strong ion-surface coupling at close distances, the electron recapture by the moving ion from the Cu(111) surface state is of course a real effect and is included in the present formalism. Also, in general, the neglect of Pauli blocking tends to increase the neutralization of incident H^- ions. Since this overneutralization will induce further recapture, this deficiency in our calculation is in part compensated. We thus expect that our time-resolved studies contribute to the improved understanding of charge transfer in surface interactions with negative ions.

1. Ion-survival probabilities

We consider H^- ions with an initial kinetic energy of 50 eV approaching the surface at various angles from an asymptotic distance of 50 a.u. At this distance, the initially occupied H^- level overlaps with image states. Owing to the improper initial conditions at the start of the propagation, the initial wave packet artificially populates these states. However, we found by visualizing the wave-packet probability density, that this loss is very small. The ions reflect specu-

larly from the surface. At each angle of incidence, Θ , with respect to the surface plane, the survival probability of the ion is calculated.

Over the whole range of Θ considered, the H^- -survival probability for the Cu(111) surface exhibits an emphatic minimum at about $\Theta_{min}=15^\circ$ (0.05% survival) (Fig. 7). Below this angle, the ion survival tends to show a sharp rise with decreasing Θ . However, moving above Θ_{min} , the survival probability gradually increases, reaching about 7.5% at normal incidence ($\Theta=90^\circ$). Similarly, for Cu(100) too, while the survival probability is 2.8% at $\Theta=90^\circ$, a very weak indication of a minimum occurs at about $\Theta_{min}=10^\circ$ (0.0003%). In general, the H^- survival for Cu(111) is always higher than for Cu(100). This difference increases on either side of Θ_{min} .

We now explain the dominant neutralization mechanism above and below Θ_{min} for both surfaces. For a given initial kinetic energy of the projectile, v_{nor}^{in} increases with the increase of Θ . This has two direct consequences: (i) a decrease in D_{cls} and (ii) a reduction of the ion-surface effective interaction time (see Table I, where we define this quantity as the total time the ion spends at $D \leq 10$). The former enables the ionic affinity level to move energetically closer to the metal conduction band and/or the image states, leading to their increased population by the ion. Our fixed-ion results [see Figs. 5(a) and 6(a)] support this, since for the surface-repelled slowly moving ion the adiabatic condition holds.

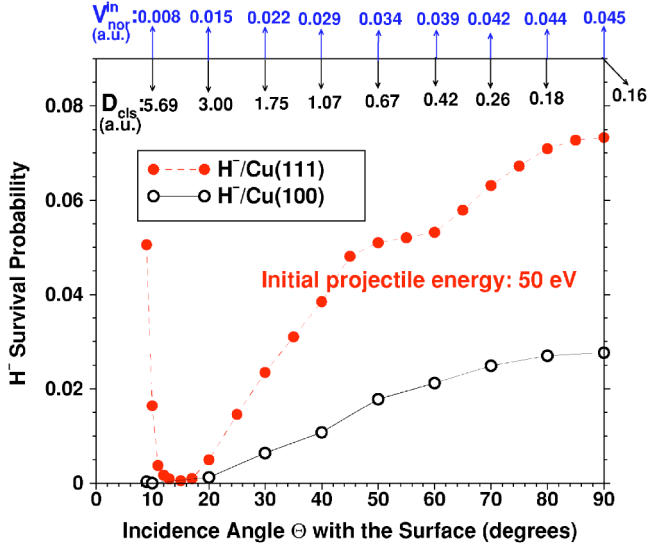


FIG. 7. (Color online) Survival probability of H^- scattered from Cu(111) and Cu(100) surfaces as a function of the incidence angle with respect to the surface plane. The initial energy of H^- is 50 eV. Initial normal velocities $v_{\text{nor}}^{\text{in}}$ and distances of closest approach, D_{cls} , are given along the upper x axis.

The second consequence, on the other hand, decreases the ion's effective electron loss to the substrate states. For higher values of Θ the interaction-time effect becomes progressively dominant. This is because the change in ensuing D_{cls} becomes so slow with increasing Θ that its effect on the dynamics remains largely unaltered for large values of Θ (see the upper x axis in Fig. 7). Therefore, the larger Θ , the shorter is the interaction time, and consequently the higher is the H^- survival. This mechanism describes the monotonically increasing survival probability with increasing Θ above Θ_{min} for both (111) and (100) surfaces. Conversely, below Θ_{min} , while the ion-surface interaction time increases (Table I), the consequent increase in D_{cls} is so rapid that the latter becomes dominating.

We apply the time-energy uncertainty relation to ascertain that the character of the main interactions is predominantly adiabatic [39]. The interaction times listed in Table I are much longer than the inverse of the energy gap at the avoided crossings of surface-state and affinity-level resonances for both Cu(111) [Fig. 5(a)] and Cu(100) [Fig. 6(a)]. Fixed-ion (adiabatic) results, therefore, provide useful insights into understanding features of the H^- -survival process. It can be noted from Figs. 5(b) and 6(b) that the *combined* decay width of the affinity-level and surface-state resonances is the largest at about $D=4$ and 5.5, respectively, for Cu(111) and Cu(100). These values, being approximately equal to the

TABLE I. Ion-surface interaction times T , as defined by the time the ion spends at $D \leq 10$ a.u., as a function of the angle of incidence Θ

Θ (deg)	90	80	70	60	50	40	30	20	10
T (a.u.)	502	509	533	578	645	759	930	1244	1855

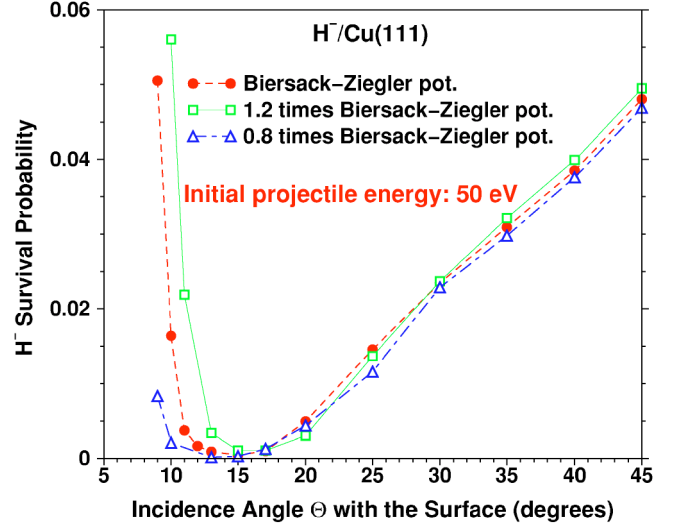


FIG. 8. (Color online) Survival probability of H^- scattered from the Cu(111) surface as a function of the incidence angle with respect to the surface plane. Along with the result for Biersack-Ziegler potential (as in Fig. 7), results for a scaled-up and a scaled-down Biersack-Ziegler potentials are also shown. The initial energy of H^- is 50 eV.

resulting D_{cls} for $\theta=15^\circ$ and 10° incidence, respectively, justify the occurrence of corresponding survival minima at these angles. As is also seen in Figs. 5(b) and 6(b), the reduction of this *combined* width with increasing D explains the increase in the survival probability with increasing D_{cls} as Θ moves below Θ_{min} .

The surface-localizing reflectivity of Cu(111) retains significant electronic probability density close to the surface and facilitates recapture by the ion. The comparability of ion-surface interaction times (Table I) with adiabatic lifetimes of the surface-state resonance ranging from a few hundreds to 2500 points to the importance of this mechanism. This recapture effect is responsible for the higher ion survival, in general, and the dramatic increase in the survival below Θ_{min} , in particular, for the Cu(111) surface (Fig. 7). In a separate calculation we found that for more energetic 1-keV ions, the shorter interaction time enhances the importance of this effect [39].

Our modeling of the classical projectile trajectory based on interatomic Biersack-Ziegler potentials (Sec. II C) is an approximation and introduces uncertainties in determining D_{cls} . In order to assess the influence of these uncertainties, we compare in Fig. 8 survival probabilities for Cu(111) from scaled potentials (a) $U^{\text{BZ}^+}=1.2 \times U^{\text{BZ}}$ and (b) $U^{\text{BZ}^-}=0.8 \times U^{\text{BZ}}$ with unscaled results of Fig. 7. Table II lists D_{cls} as determined by the trajectories. Quantitative differences between predictions of the trajectories are prominent at lower angles. As expected, the position of survival minimum Θ_{min} shifts to larger angles with the increase of interaction strength at close distances. This confirms our conclusion that D_{cls} is the major determinant of the mechanism below Θ_{min} . For larger angles, the ion-survival probability is rather insensitive to the $\pm 20\%$ changes in the strength of U^{BZ} . This is because the interaction time, which determines the survival in this range, changes very little from one trajectory to an-

TABLE II. Distances of closest approach, D_{cls} , for unscaled and scaled Biersack-Ziegler interaction potentials versus Θ .

Θ (deg)	90	80	70	60	50	40	30	20	10
$D_{\text{cls}}^{\text{BZ}}$ (a.u.)	0.16	0.18	0.26	0.42	0.67	1.07	1.75	3.00	5.69
$D_{\text{cls}}^{\text{BZ}+}$ (a.u.)	0.32	0.35	0.44	0.60	0.87	1.31	2.03	3.33	6.08
$D_{\text{cls}}^{\text{BZ}-}$ (a.u.)	0.00	0.01	0.08	0.21	0.44	0.81	1.44	2.61	5.22

other for such slow ions. In general, the shape of the curves being identical implies that the same physics of interaction can be expected for a more accurate trajectory.

In order to visualize in further detail the mechanisms responsible for different ion survivals in collisions with the Cu(111) and Cu(100) surface, we now examine some typical “snapshots” of the wave-packet propagation.

2. Wave-packet diagnosis

Results for 60° ion incidence are displayed in Fig. 9. In Fig. 9(a), for $D=2.76$, strong surface localization is evident for Cu(111). The wave-packet spreads and clear nodal structures from the quantum interference (Sec. III A 2) emerge symmetrically along the parallel direction outside the surface. Since the populated surface state at this distance is energetically close to the valence band [Fig. 5(a)], the “beads” decay into the valence band by forming “jets.” Electrons in the central jet have small parallel velocity. A steady increase of the parallel velocity is evidenced going symmetrically away from the center in the parallel direction.

Note that from either edge ($x=\pm 15$) of the central bead emanate several overlapping jets of slightly different parallel velocity, forming a broad structure. The tangent of the average angle, which each of these symmetric structures makes with the surface, provides an estimate of the ratio $k_{\text{nor}}/k_{\text{par}} \sim 0.62$, where k_{nor} is the electron normal velocity. In the Cu(100) panel of the same figure the formation of nodal structures is insignificant while very strong decay into the valence band is dominant. A rather diffused distribution of electrons appears inside the bulk on two symmetric decay trails. This hints at the decay of the embedded surface state of Cu(100) where the main decay trails appear closer to the surface normal. The corresponding $k_{\text{nor}}/k_{\text{par}} \sim 1.25$ roughly indicates a normal decay velocity (relative to the parallel decay velocity) twice as large as for Cu(111).

In Fig. 9(b), the ion arrives roughly at the distance of closest approach, 0.5. Here the adiabatic energy position of the affinity-level resonance moves very close to the conduction band of Cu(111) [Fig. 5(a)]. The shape of the wave-packet density is dominated by a strong decay into the conduction band as well as by the subsequent population of the image states (the bulging central structure on the vacuum side of the projectile). For Cu(100), on the other hand, since the affinity level decays only through image states [Fig. 6(a)], a stronger diffusion towards the vacuum occurs. The remnants of the density from earlier decay into the bulk are seen being absorbed at the grid edges while virtually no new decay in the valence band is seen.

Figure 9(c) presents the electronic probability density at $D=6.59$ on the outward excursion of the ion. For Cu(111), a

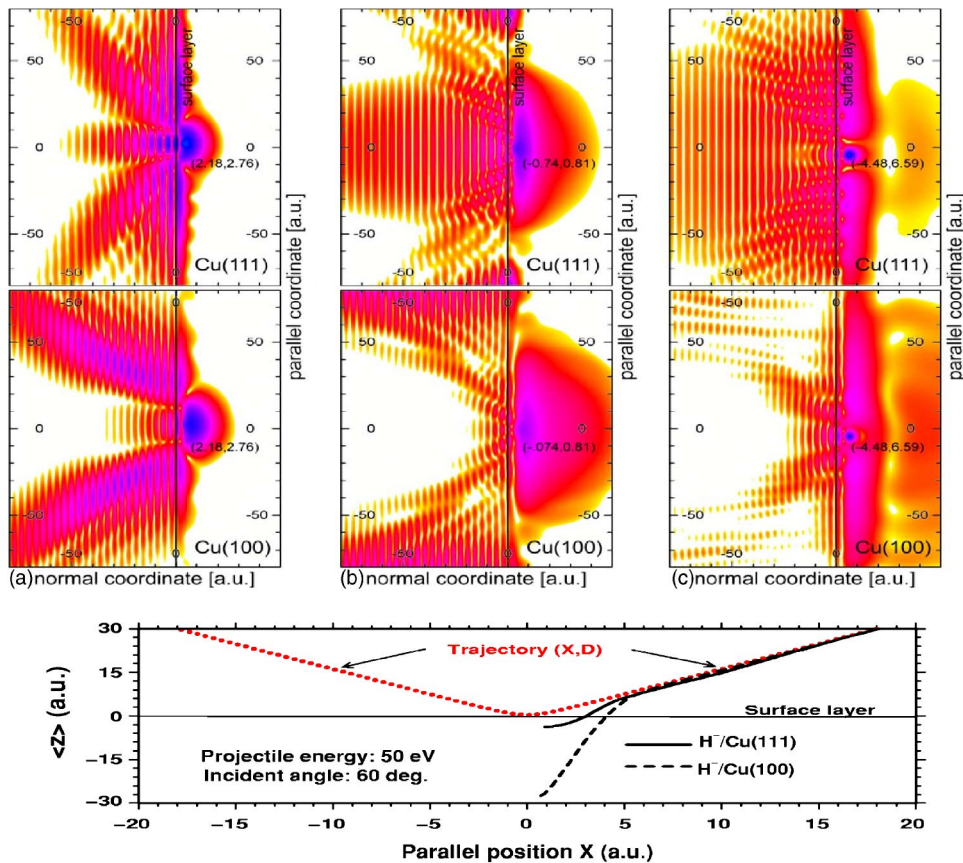


FIG. 9. (Color online) Wave-packet densities (in logarithmic scale) for Cu(111) (upper panel) and Cu(100) (lower panel) at times -110 a.u. (a), 20 a.u. (b), and 180 a.u. (c), relative to the time at which the point of closest approach is reached. The ion approaches the surface at an angle of 60° with respect to the surface and with an energy of 50 eV. Positions (X, D) are given in parentheses, with X being relative to the point of closest approach. Bottom panel: the expectation value of z as a function of the parallel position X of the ion along the trajectory (shown).

pronounced tendency of retaining density near the surface results in the reformation of the nodes along the surface, forming decay jets in the valence band. Subsequently, enhanced recapture by the projectile, leading to a high probability density near the projectile nucleus, occurs. The previously populated first image state (seen as a high-density region up to $z \sim 15$ in the vacuum) has spread in the surface plane and is seen decaying via the conduction band into the bulk. Higher image states appear as a faint outgoing blob farther away from the surface as a result of their relatively rapid decay into the degenerate conduction band. In contrast, for Cu(100), the strongly populated first (up to $z \sim 15$ a.u.) and second image state evolve into the vacuum. This moves the charge density away from the surface considerably reducing the recapture probability.

The bottom panel of Fig. 9 provides the normal position $\langle z \rangle$ of the center of gravity of the wave packet as the ion approaches the surface. At very large distances it roughly coincides with the position of the ion, as expected. In the interaction region the penetration into Cu(100) is much higher, reaching about -30 near D_{cls} as opposed to -4 for Cu(111).

IV. CONCLUDING REMARKS

To conclude, we have demonstrated significant accumulation of charge density near the surface during resonant neutralization of H^- near a model Cu(111) surface by directly analyzing the evolution of the active electron's wave packet. In contradistinction, Cu(100) exhibits a very efficient electron decay channel through the metal valence band. The key to this difference, as shown, is a *localizing* reflectivity of the (111) band gap along the surface normal. The image states for both surfaces are populated by the ion at close distances. However, the evolution and decay of these states are found to be very different for Cu(111) and Cu(100). While for Cu(111) the image states decay through the metal conduction

band, for Cu(100) they cause the charge density to move away from the surface on the vacuum side. Consequently, clear differences are seen between the neutralization rates of H^- scattered from Cu(111) and Cu(100) surfaces. The competing influence of the ion-surface interaction time and the distance of closest approach leads to a minimum in the ion-survival probability as a function of the incidence angle.

We have restricted the active electron to move in the scattering plane of the ion, thereby reducing the dimensionality of the model surface from two to one. Nevertheless, we expect that the main characteristics of the charge-transfer processes analyzed in this work are not affected by the reduction of dimensionality. In a full 3D calculation, we expect the ion neutralization rate to increase roughly by a factor of 2. In recent 2D calculations for the neutralization of H^- near Ag(111), we found good agreement with experimental ion-survival probabilities by including 3D effects merely through an extra factor of 2 in (2D) transition rates [39]. Further, we do not expect the inclusion of surface corrugations to alter our main conclusions, since RCT is predominantly mediated by transfer along the surface normal. However, such a real 3D potential will provide a more complete account of the process by, for example, including the parallel velocity effects for grazing ion-surface scattering [9,38].

A more severe limitation of the present calculation is the lack of a consistent inclusion of quantum statistical effects in the one-electron frame. Proper accounting of level occupations and implementation of the Pauli exclusion principle were beyond the scope of this work and constitute a formidable future challenge.

ACKNOWLEDGMENTS

This work is supported by NSF (Grant No. PHY-0071035) and the Division of Chemical Sciences, Office of Basic Energy Sciences, Office of Energy Research, U.S. DOE.

-
- [1] J. P. Gauyacq, A. Borisov, and D. Teillet-Billy, in *Formation/ Destruction of Negative Ions in Heavy Particle-Surface Collisions*, edited by V. Esaulov (Cambridge University Press, Cambridge, England, 1996).
 - [2] H. Shao, D. C. Langreth, and P. Nordlander, in *Low Energy Ion-Surface Interactions*, edited by J. W. Rabalais (Wiley, New York, 1994), p. 118; J. J. C. Geerlings and J. Los, Phys. Rep. **190**, 133 (1990).
 - [3] S. Wethekam, A. Mertens, and H. Winter, Phys. Rev. Lett. **90**, 037602 (2003).
 - [4] S. B. Hill, C. B. Haich, Z. Zhou, P. Nordlander, and F. B. Dunning, Phys. Rev. Lett. **85**, 5444 (2000).
 - [5] S. Ustaze, R. Verucchi, S. Lacombe, L. Guillemot, and V. A. Esaulov, Phys. Rev. Lett. **79**, 3526 (1997).
 - [6] A. Robin, D. Niemann, N. Stolterfoht, and W. Heiland, Phys. Rev. A **67**, 052901 (2003).
 - [7] Y. Yang and J. A. Yarmoff, Phys. Rev. Lett. **89**, 196102 (2002).
 - [8] L. Guillemot and V. A. Esaulov, Phys. Rev. Lett. **82**, 4552 (1999).
 - [9] T. Hecht, H. Winter, A. G. Borisov, J. P. Gauyacq, and A. K. Kazansky, Phys. Rev. Lett. **84**, 2517 (2000).
 - [10] E. Sanchez, L. Guillemot, and V. A. Esaulov, Phys. Rev. Lett. **83**, 428 (1999).
 - [11] S. Ustaze *et al.*, Surf. Sci. **415**, L1027 (1998).
 - [12] M. Maazouz, A. G. Borisov, V. A. Esaulov, J. P. Gauyacq, L. Guillemot, S. Lacombe, and D. Teillet-Billy, Phys. Rev. B **55**, 13 869 (1997).
 - [13] F. Wyputta, R. Zimny, and H. Winter, Nucl. Instrum. Methods Phys. Res. B **58**, 379 (1991).
 - [14] J. Los and J. J. C. Geerlings, Phys. Rep. **190**, 133 (1990).
 - [15] A. G. Borisov, A. K. Kazansky, and J. P. Gauyacq, Phys. Rev. Lett. **80**, 1996 (1998).
 - [16] A. G. Borisov, A. K. Kazansky, and J. P. Gauyacq, Phys. Rev. B **59**, 10 935 (1999).
 - [17] P. J. Rous, Phys. Rev. Lett. **74**, 1835 (1995).

- [18] M. Bauer, S. Pawlik, and M. Aeschlimann, *Phys. Rev. B* **60**, 5016 (1999).
- [19] A. G. Borisov, J. P. Gauyacq, A. K. Kazansky, E. V. Chulkov, V. M. Silkin, and P. M. Echenique, *Phys. Rev. Lett.* **86**, 488 (2001).
- [20] S. Ogawa, H. Nagano, and H. Petek, *Phys. Rev. Lett.* **82**, 1931 (1999).
- [21] J. F. Zhu, H. Ellmer, H. Malissa, T. Brandstetter, D. Semrad, and P. Zeppenfeld, *Phys. Rev. B* **68**, 045406 (2003).
- [22] B. Lehner, M. Hohage, and P. Zeppenfeld, *Phys. Rev. B* **65**, 165407 (2002).
- [23] E. Bertel, *Surf. Sci.* **367**, L61 (1996).
- [24] B. Bahrim, D. Teillet-Billy, and J. P. Gauyacq, *Surf. Sci.* **431**, 193 (1999).
- [25] P. Nordlander, *Phys. Rev. B* **46**, 2584 (1992).
- [26] B. Bahrim and U. Thumm, *Surf. Sci.* **521**, 84 (2002); P. Kürpick and U. Thumm, *Phys. Rev. A* **58**, 2174 (1998).
- [27] F. Martin and M. F. Politis, *Surf. Sci.* **356**, 247 (1996).
- [28] U. Thumm, in *Book of Invited Papers, XXII International Conference on Photonic, Electronic, and Atomic Collisions, Santa Fe, NM*, edited by J. Burgdörfer, J. S. Cohen, S. Datz, and C. R. Vane (Rinton Press, Princeton, 2002), p. 592.
- [29] W. H. Press, S. A. Teukolsky, W. T. Vetterling, and B. P. Flannery, *Numerical Recipes in FORTRAN* (Cambridge University Press, Cambridge, England, 1993).
- [30] S. Yoshida, S. Watanabe, C. O. Reinhold, and J. Burgdörfer, *Phys. Rev. A* **60**, 1113 (1999).
- [31] E. V. Chulkov, V. M. Silkin, and P. M. Echenique, *Surf. Sci.* **437**, 330 (1999).
- [32] T. Klamroth, P. Saalfrank, and U. Höfer, *Phys. Rev. B* **64**, 035420 (2001).
- [33] P. J. Jennings, R. O. Jones, and M. Weinert, *Phys. Rev. B* **37**, 6113 (1988).
- [34] J. S. Cohen and G. Fiorentini, *Phys. Rev. A* **33**, 1590 (1986).
- [35] V. A. Ermoshin and A. K. Kazansky, *Phys. Lett. A* **218**, 99 (1996).
- [36] J. P. Biersack and J. F. Ziegler, *Nucl. Instrum. Methods Phys. Res.* **194**, 93 (1982); J. Ducreé, H. J. Andrä, and U. Thumm, *Phys. Rev. A* **60**, 3029 (1999).
- [37] J. Burgdörfer, E. Kupfer, and H. Gabriel, *Phys. Rev. A* **35**, 4963 (1987).
- [38] H. Winter, *Comments At. Mol. Phys.* **26**, 287 (1991).
- [39] H. Chakraborty, T. Niederhausen, and U. Thumm, *Phys. Rev. A* **69**, 052901 (2004).